A&A, 711, A223 (2026)
https://doi.org/10.1051/0004-6361/202659077

Astronomy & Astrophysics

Spectral-temporal analytical model for telescope dome-seeing

P. Martinez⋆

Université Côte d'Azur, Observatoire de la Côte d'Azur, CNRS, Laboratoire Lagrange, France

Received 22 January 2026 / Accepted 15 June 2026

ABSTRACT

Context. Turbulence inside telescope domes, commonly referred to as dome-seeing, can significantly degrade image quality, especially for large-aperture facilities such as the extremely large telescopes. Unlike free-atmosphere turbulence, dome-seeing results from complex interactions between thermal gradients, slow internal air motion, mechanical structures, and localized convective plumes. Although dome-seeing has been recognized as a critical source of wavefront aberrations, no standard physically motivated model currently exists for generating controlled, reproducible phase screens representative of dome conditions.

Aims. We aimed to build a physically interpretable and numerically efficient model capable of reproducing the spatial and temporal characteristics of dome-induced turbulence. The objective was to generate synthetic phase screens that parametrize key mechanisms, such as large-scale thermal gradients, small-scale convection, mechanical perturbations, slow advection, rotational drift, and stochastic boiling, using a compact set of tunable parameters suitable for end-to-end telescope simulations.

Methods. We introduce a hybrid Fourier-domain model in which the spatial power spectral density (PSD) is the sum of (i) a sub-Kolmogorov power-law component, (ii) a high-frequency enhancement term motivated by gradient-driven fluctuations, and (iii) a Gaussian bump that models intermediate convection scales. Temporal evolution is constructed via a scale-dependent autoregressive process combined with slow advection, a spiral rotation of the flow, and stochastic boiling noise whose amplitude is chosen to maintain stationary variance in each Fourier mode.

Results. The model is modular and parameterized by physically grounded quantities, enabling the exploration of a broad range of dome-seeing PSD behaviors. In particular, it reproduces several characteristics expected for local dome turbulence, including shallow PSD slopes, enhanced high-frequency content, and de-correlation times of a few seconds.

Conclusions. The proposed model provides a first physics-guided and tunable framework for simulating dome-seeing with realistic spatial and temporal behavior. Designed for end-to-end adaptive-optics and high-contrast imaging simulations, the framework aims to bridge empirical observations and turbulence theory for next-generation observatories, although the practical calibration and experimental validation of the proposed parameterization remain to be demonstrated.

Key words. turbulence – instrumentation: adaptive optics – instrumentation: high angular resolution – methods: numerical – techniques: high angular resolution – telescopes

1. Introduction

The performance of modern large telescopes increasingly depends on the control and mitigation of local turbulence generated within the enclosure. Although telescope dome-seeing has been recognized for decades (e.g., Woolf 1979; Racine et al. 1991), it remains far less characterized than atmospheric seeing (e.g., Tatarskii 1961; Young 1974; Roddier 1981; Racine et al. 1991; Tokovinin 2023), which has been the subject of extensive observational and theoretical studies.

Dome-generated turbulence is produced inside the enclosure by thermal gradients, mechanically driven flows, structural obstacles, and ventilation patterns. As a result, despite its significant impact on image quality and adaptive optics (AO) performance, dome-seeing continues to be one of the least understood contributors to the optical error budget of large telescopes. For extremely large telescopes (ELTs), whose enclosures reach dimensions of 80–100 m, dome-induced aberrations can represent a significant fraction of the total wavefront error, with direct implications for AO performance, calibration stability, and image quality during both daytime operations and nighttime science observations.

Dome-seeing arises from a complex interplay of thermally driven convection, slow bulk flows, shear layers, and small-scale fluctuations produced by local heat sources (electronics, cable runs, and motors) and residual warm air stored in the dome cavity. These processes generate turbulent structures on spatial scales ranging from a few centimeters to several tens of meters, with temporal evolution significantly slower than that expected from fully developed atmospheric turbulence.

Existing parametric models, usually based on Kolmogorov (Kolmogorov 1941) or von Kármán statistics (Tatarskii 1961; Ziad et al. 2000; Tokovinin et al. 2007; Ziad et al. 2012), do not capture the non-Kolmogorov behavior, long correlation times, or multicomponent nature of dome turbulence. As a result, AO performance models and end-to-end simulations often lack a realistic representation of the dome contribution, limiting the accuracy of point spread function (PSF) predictions and turbulence forecasting tools.

Several observational studies have reported departures from atmospheric-like statistics inside domes, including shallower spectral slopes, increased power at intermediate spatial frequencies, and highly anisotropic and slowly evolving flow fields (Bustos & Tokovinin 2018; Lai et al. 2019a,b; Tallis et al. 2020; Munro et al. 2023). However, a physically motivated, flexible, and numerically efficient model capable of reproducing these characteristics has not yet been adopted by AO simulation frameworks. Such a model is critically needed for upcoming ELTs, whose unprecedented enclosure sizes and thermal

⋆ Corresponding author: patrice.martinez@oca.eu

environments call for predictive tools that can inform dome ventilation strategies, telescope thermal control, AO system designs, and high-contrast imaging instrument strategies (Tallis et al. 2018, 2020).

A dome-seeing phase-screen generator based on power spectral densities (PSDs) is particularly valuable for AO end-to-end simulations and high-contrast imaging studies, where the atmospheric turbulence is already modeled through Fourier-domain statistics of AO residuals (e.g., Rigaut et al. 1998; Jolissaint & Veran 2002; Le Louarn et al. 2004; Carbillet & Riccardi 2010; Gratadour et al. 2014; Jia et al. 2015; Carbillet et al. 2016; Agapito et al. 2016; Por et al. 2018; Ferreira et al. 2018; Guyon et al. 2018; Fétick et al. 2019). Incorporating dome-seeing with a similarly PSD-driven approach ensures full spectral continuity between atmospheric and internal turbulence sources, enabling realistic predictions of image quality, temporal speckle behavior, and instrument performance. Such compatibility is especially important for extreme-AO systems and coronagraphic instruments, for which the high-spatial-frequency content and slow temporal evolution of dome-driven aberrations can dominate the final contrast budget and thus calls for proper modeling. PSD-based phase screens therefore provide a flexible, analytically controlled, and computationally efficient way to inject physically consistent dome-seeing signatures into AO performance simulations.

In this work, we introduce a new physically grounded model for dome-seeing phase screens, combining a three-component PSD with a time-evolution law that captures the slow advection, exponential de-correlation, and stochastic boiling characteristic of dome turbulence. The PSD formulation allows for the coexistence of large-scale convective structures, intermediate-scale thermal plumes, and fine-scale mechanical and/or thermal noise, while the temporal update scheme provides a statistically stationary process with realistic correlation times and flow patterns in large telescope enclosures.

The purpose of this paper is to present the full mathematical framework and describe the physical motivation for each term, suitable for AO end-to-end simulators or PSF prediction pipelines. Our model provides the possibility to generate statistically consistent multilayer screen ensembles. This work therefore aims to bridge the gap between empirical measurements, turbulence physics, and numerical simulations, providing a practical and physically interpretable tool for the next generation of large telescopes.

Section 2 reviews the known spatial and temporal characteristics of dome-seeing as inferred from observational data analyses. Section 3 provides an overview of existing approaches used to model or monitor dome-seeing, including their respective strengths and limitations. In Sect. 4 we introduce our analytical framework for generating phase screens that reproduce the spatial and temporal signatures of dome-seeing turbulence. Finally, Sect. 5 summarizes our conclusions.

2. Dome-seeing from observational data analysis

Over the past decades, several observational studies have provided a coherent, though still incomplete, picture of the physical properties of dome-seeing in large astronomical enclosures. Despite the diversity of telescopes, instruments, and diagnostic methods, a number of robust trends emerge. Observational studies conducted on a wide range of telescopes, from 1–4 m class instruments (Racine et al. 1991; Bustos & Tokovinin 2018; Lai et al. 2019a; Kurmus et al. 2023; Benedict 2024; Kornilov et al. 2025; Marangola et al. 2025) to the current generation of 8–10 m facilities (Vogiatzis et al. 2018; Tallis et al. 2020; Munro et al. 2023; Osborn & Alaluf 2023; Ogane et al. 2024), consistently show that dome-seeing arises from low-speed, thermally driven airflow inside the enclosure. Its signature differs markedly from atmospheric turbulence above the dome, both in spatial and temporal behavior. The analysis of wavefront sensor telemetry, differential image motion, temperature gradients, and in situ anemometry provides a coherent set of characteristics that inform the physical modeling implemented in the present work.

First, the spatial structure of dome-induced wavefront errors is dominated by very low frequencies, with most of the variance contained at scales of several meters to tens of meters. This behavior reflects the geometry of the enclosure: temperature differences between the primary mirror, the telescope structure, and the surrounding air generate large-scale buoyant cells and slowly drifting plumes. At the same time, finer structures are frequently observed, often associated with ventilation openings, warm cable ducts, electronics racks, or mirror cell heat sources. These intermediate-scale features introduce secondary bumps or excess power at spatial frequencies higher than those predicted from classical Kolmogorov turbulence (Lai et al. 2019a,b), motivating the use of multicomponent PSDs in the modeling. From the morphological analysis of stacked PSFs from the Canada-France-Hawaii observatory (CFHT) and the University of Hawaii 2.2 m telescope (UH88), Lai et al. (2019a,b) inferred estimates of the Fried parameter and outer scale (r_0 and L_0, respectively), and concluded that the turbulence contains a substantial amount of high-spatial-frequency power, as indicated by the strong PSF wings and the apparent reduction of the effective outer scale, a signature consistent with significant dome-seeing contributions. In Tallis et al. (2020), the authors examine the characteristics of dome-seeing using the Gemini Planet Imager instrument, installed at the Gemini South Observatory, by calculating the PSD of spatial and temporal Fourier modes. The study shows that turbulence created by a warm primary mirror deviates from the standard atmospheric models assumed in AO.

Second, the temporal evolution of dome-seeing is extremely slow (Nicolas et al. 1998). Wind speeds measured in domes typically lie between 0.02 and 0.2 $\mathrm{m\,s^{-1}}$, far below external wind velocities. Correspondingly, wavefront sensor cross-correlation analyses reveal de-correlation times of several seconds, occasionally exceeding 10s in well-controlled thermal conditions. These observations rule out frozen-flow assumptions alone and indicate that dome turbulence contains both advected structures and non-advective boiling components that evolve intrinsically due to weak convection and thermal relaxation. The relative contributions of these two processes vary with the thermal environment: daytime residual heat leads to stronger intrinsic evolution, while nighttime ventilation introduces small but coherent advective flows. In Tallis et al. (2020), the authors show that the temporal behavior departs from the usual frozen-flow assumption: rather than being carried steadily across the telescope by wind at a single speed, the turbulence above the mirror evolves locally, with slower, non-advected fluctuations. These deviations mean that dome-seeing turbulence is less predictable for AO control systems and can therefore degrade high-contrast imaging performance more severely than typical atmospheric turbulence would.

Third, the strength of dome-seeing correlates strongly with temperature gradients inside the dome. A mirror-air temperature difference as small as 1–2°C is sufficient to generate tens of nanometers RMS of wavefront error (Tallis et al. 2020). Poor ventilation, residual heat stored in structural elements, or localized hot spots (electronics, cable runs, hydraulic actuators) significantly amplify the turbulence. Observations during daytime cool-down or after rapid weather changes reveal a characteristic increase in small-scale structures, suggesting enhanced local convection rather than large-scale stratification.

Altogether, the collected observational evidence identifies dome-seeing as a hybrid turbulent process, governed by slow advection, internal thermal relaxation, and mechanically or thermally generated fine-scale structures. It confirms that dome-seeing is an internal turbulence phenomenon rather than a truncated extension of free-atmosphere turbulence (e.g., Pazder et al. 2008; Zhang et al. 2023; Conan et al. 2024). These empirical constraints directly guide the modeling choices presented in this work: multicomponent PSDs, exponentially de-correlating temporal modes, very low wind speeds, and parameterized stochastic noise to represent non-advective boiling. The consistency between these observational properties and the behavior reproduced by the model provides the physical basis for its use in end-to-end AO simulations and dome control studies.

Overall, observational evidence supports a picture in which dome-seeing arises from a combination of: (i) large-scale convection cells driven by thermal gradients within the enclosure, (ii) intermediate-scale structures associated with localized heating or mechanical elements, (iii) weak high-frequency fluctuations introduced by ventilation or instrument-level thermal sources, and (iv) temporal evolution dominated by slow de-correlation and minimal advection.

3. Dome-seeing modeling tool and limitations

A variety of tools and methodologies have been developed to characterize or model turbulence inside telescope enclosures. These approaches can be broadly grouped into three families: (i) statistical models derived from long-term monitoring, (ii) thermal-energy-balance models describing temperature-driven flow generation, and (iii) computational fluid dynamics (CFD) simulations of dome aerodynamics. Although each method provides valuable physical insights, none is directly suited to generating the phase-screen time series required for AO simulations. In this section we review their characteristics and identify the limitations that motivate the development of a dedicated statistical-physical dome-seeing model.

3.1. Statistical characterization from monitoring data

Many observatories operate extensive networks of temperature sensors, airflow probes, anemometers, differential temperature monitors, or dedicated instruments mounted on or near the telescope structure (Lai et al. 2016, 2019a; Kurmus et al. 2023; Munro et al. 2023; Benedict 2024; Ogane et al. 2024). These datasets have been used to derive empirical relations between dome thermal gradients, ventilation efficiency, and image degradation. Time-series analyses often reveal long correlation times (on the order of seconds), extremely low flow speeds ($\sim$0.01–0.2 m s^{-1}), and the presence of quasi-stationary convection cells. These systems are designed to map turbulence locally in or around telescope domes, to provide a quantitative measurement for controlling the dome ventilation valves, and to study effects that are harmful to image quality (such as the low-wind effect Milli et al. 2018). However, such monitoring-based models do not provide a generative description of the turbulence itself. They typically lack spatial information and contain no spectral content, making them unsuitable for producing phase screens or realistic AO inputs. Furthermore, monitoring systems differ from facility to facility and often have limited temporal resolution, leading to significant uncertainties in the inferred turbulence statistics.

3.2. Thermal and energy-balance models

Thermal models describe how heat is exchanged between the telescope structure, mirror, enclosure air, and the external atmosphere (Yang et al. 2022). They are effective for understanding bulk temperature evolution, mirror-air lag, and the conditions that trigger convection plumes or stratification. These models can reproduce the overall magnitude of thermal disequilibrium, which correlates with the strength of dome-seeing. However, they do not resolve the internal turbulent cascade, nor do they provide information on the PSD or temporal de-correlation of phase fluctuations. Without resolving the interplay between thermal gradients, local buoyancy instabilities, and small-scale shear layers, such models cannot generate the spatially and temporally structured turbulence required by AO simulations.

3.3. CFD and aerodynamics-based simulations

Computational fluid dynamics (CFD) has been employed to model airflow in and around telescope enclosures, especially for next-generation facilities (Basden et al. 2015; Li et al. 2019; Zhang et al. 2024; Fitzpatrick et al. 2024; Conan et al. 2024). CFD can capture the effects of dome geometry, venting strategy, mirror heating, and wind coupling. It provides unparalleled insight into the global flow patterns, including recirculation regions, stratification layers, shear zones, and thermally driven convection. Despite this, CFD-based approaches have several limitations for AO purposes: (i) they are computationally expensive, often requiring millions of mesh elements to resolve meter- and decimeter-scale structures; (ii) they cannot realistically reach the centimeter or sub-centimeter scales that dominate phase fluctuations at optical wavelengths; and (iii) the temporal sampling is typically limited to milliseconds or longer, insufficient to reproduce the second-scale de-correlation behavior observed in real domes. Moreover, CFD simulations are highly sensitive to boundary conditions and thermal forcing, and they are not easily tuned to match measured PSD slopes, small-scale convection, or observed spatial anisotropies.

3.4. Limitations for AO-oriented phase-screen generation

Across all three families of models, a common issue is that none directly produces high-resolution, statistically consistent phase screens with realistic temporal evolution. AO simulators require spatial PSDs over several decades of scale, smooth transitions between inertial and high-frequency regimes, and physically motivated de-correlation laws. Monitoring-based statistics lack spatial content; thermal models do not resolve the turbulent cascade; CFD cannot reach the spatial and temporal scales relevant for AO. These limitations underscore the need for a dedicated statistical-physical model that combines observational constraints, plausible physical mechanisms, and generative capability. Such a model must reproduce both the spatial PSD of dome turbulence and its characteristic slow temporal evolution, while allowing the parametrization of multiple layers, each representing a distinct physical component of the dome environment.

4. Dome-seeing analytical model

In this section we describe the spatial and temporal modeling used to generate synthetic phase screens emulating of dome-seeing turbulence. The method combines (i) a flexible PSD, and (ii) a time-evolution equation based on an autoregressive (AR) process with advection, slow spiral rotation, and stochastic non-translational boiling. This approach is designed to reproduce the experimentally observed behavior of dome turbulence: long-lived large scales, weak translation, significant small-scale de-correlation, and non-Kolmogorov power laws.

4.1. Spatial power spectral density

The spatial structure of each phase screen is determined by prescribing an azimuthally symmetric 2D PSD as a function of the radial spatial frequency, denoted k, as

$$k = \sqrt{f_x^2 + f_y^2}, \tag{1}$$

where f_x and f_y denote the spatial frequencies (in cycles per meter) along the x-direction and y-direction, respectively. The PSD used is the sum of three components:

$$\begin{aligned} \mathrm{PSD}(k) = &\left[\beta_0 \left(k^2 + k_{\mathrm{out}}^2\right)^{\alpha/2} + \beta_{\mathrm{HF}} \left(k^2 + k_{\mathrm{out}}^2\right)^{(\alpha-2)/2}\right] \\ &\times \exp\left[-\left(\frac{k}{k_{in}}\right)^2\right] \\ &+ \beta_{bump} \exp\left[-\frac{1}{2}\left(\frac{k-k_0}{\sigma_k}\right)^2\right], \end{aligned} \tag{2}$$

where α is the power-law slope controlling the large-scale behavior, β_{HF} sets the amplitude of the high-frequency tail, k_0 and σ_k describe a Gaussian "bump" representing excess power at intermediate scales, consistent with measurements of dome-seeing. $k_{\mathrm{out}} = 2\pi/L_0$ defines the cutoff spatial frequency associated with an outer scale, denoted L_0, introducing a flattening of the spectrum at low spatial frequencies (small k). An inner scale l_0 can also be introduced through the cutoff spatial frequency $k_{\mathrm{in}} = 2\pi/l_0$, using an exponential damping term to suppress unphysical power at very high spatial frequencies. The coefficients β_0, β_{HF}, and β_{bump} act as scaling factors for the three contributions of the PSD (background, high-frequency enhancement, and localized spectral feature, respectively). These tuning parameters carry the units required to preserve the dimensional consistency of the PSD, with their exact dimensions depending on the adopted PSD normalization. In addition, to avoid ringing, aliasing, and PSD discontinuities at the highest sampled frequencies, a smooth taper, $T(k)$ can be applied near the Nyquist limit:

$$T(k) = \begin{cases} 1, & k \leq n\, k_{\mathrm{Nyq}}, \\ \exp\left[-\frac{1}{2}\left(\frac{k - n\, k_{\mathrm{Nyq}}}{0.05\, k_{\mathrm{Nyq}}}\right)^2\right], & k > n\, k_{\mathrm{Nyq}}, \end{cases} \tag{3}$$

where n is a dimensionless parameter ($0 < n < 1$) that specifies the fraction of the Nyquist frequency at which the tapering begins. The final PSD becomes

$$\mathrm{PSD}_{\mathrm{final}}(k) = \mathrm{PSD}(k)\, T(k). \tag{4}$$

The second term in Eq. (2), is introduced to capture an excess of high-spatial-frequency power that is often observed in dome-seeing data but not reproduced by a single pure power law. This behavior is expected in the presence of small-scale mechanical or thermal perturbations such as sharp temperature gradients, localized convective plumes, ventilator wakes, cable runs, or structural edges inside the dome. A convenient way to understand the exponent $(\alpha - 2)$ is to consider that many physical processes responsible for high-frequency power injection behave as spatial derivatives of the underlying large-scale turbulence field. Many dome-seeing contributors (mirror-edge heating, mechanical fans, baffling, support structures, localized convection) generate refractive-index fluctuations proportional to spatial derivatives of temperature or velocity. A spatial derivative in physical space corresponds, in Fourier space, to multiplication by the wavenumber. Therefore, a fluctuation source proportional to a gradient introduces an amplification proportional to the norm of the wavenumber vector. Consequently, adding a high-frequency component with a k^2 scaling in amplitude corresponds, in terms of PSD, to a multiplicative factor of k^{-2} relative to the main power-law spectrum. Gradient-driven processes enhance high-frequency power: in the PSD model, this contribution is included phenomenologically through a term scaling as $k^{\alpha-2}$, which flattens the spectrum at large k and adds the additional small-scale power expected from mechanical and thermal boundary-layer effects.

In the third term of Eq. (2), k_0 (in cycles m^{-1}) represents the spatial frequency at which dome-induced structures inject additional power, typically associated with coherent circulation cells inside the telescope enclosure. The parameter σ_k controls the spectral width of the Gaussian bump added to the baseline power-law PSD. This bump represents excess power at an intermediate spatial scale, associated with persistent structures in dome-seeing such as thermal plumes, ventilation eddies, or localized shear layers. Laboratory measurements and on-sky dome turbulence characterizations show that these features are not narrowly peaked in spatial frequency, but instead span a moderately broad range of scales. For this reason, the values of σ_k should correspond to a physically reasonable fractional bandwidth (typically 20–40% of k_0): wide enough to avoid an unphysical, sharply localized feature in the PSD, yet narrow enough to preserve a clearly identifiable mesoscale contribution distinct from both the large-scale slope and the high-frequency tail.

4.2. Temporal evolution

The temporal behavior of the screens is designed to reproduce three observed features of dome turbulence: (i) slow advection or drift of the entire structure, (ii) small, quasi-periodic spiral motions of the flow, and (iii) rapid small-scale de-correlation ("boiling") not explained by pure frozen-flow advection. To model these effects, each Fourier component $F(k, t)$ is evolved according to an AR process (AR(1); see Appendix A for more details; Box & Jenkins 1976) with a k-dependent timescale:

$$F(k, t + \Delta t) = a(k)\, F(k, t)\, e^{-2\pi i\, \Delta t\, (f_x v_x(t) + f_y v_y(t))} + \epsilon\, \eta(k, t), \tag{5}$$

where the noise term $\eta(k, t)$ is complex, Gaussian, and independent for each Fourier mode and time-step, and where

$$\epsilon = \sqrt{1 - a(k)^2}. \tag{6}$$

In Eq. (5), the coefficient $a(k)$ represents the correlation timescale, where

$$a(k) = \exp\left(-\frac{\Delta t}{\tau(k)}\right), \tag{7}$$

Table 1. All variables used in the spatial (PSD) and temporal evolution models of dome-seeing phase screens.

Symbol	Units	Definition
k	cycles m^{-1}	Radial spatial frequency
f_x, f_y	cycles m^{-1}	Spatial frequencies in the horizontal and vertical directions of the screen
α	–	Power-law slope of the baseline turbulence spectrum
β_0	–	Global scaling factor of the quasi-static background PSD
$\beta_{\rm HF}$	–	Amplitude of the high-frequency enhancement component
$\beta_{\rm bump}$	–	Amplitude of the localized spectral enhancement
k_0	cycles m^{-1}	Central frequency of the Gaussian spectral bump representing intermediate-scale convection
σ_k	cycles m^{-1}	Spectral width of the Gaussian bump
k_{out}	rad m^{-1}	Cutoff spatial frequency associated with an outer scale L_0
k_{in}	rad m^{-1}	Cutoff spatial frequency associated with an inner scale l_0
$k_{\rm Nyq}$	cycles m^{-1}	Nyquist spatial frequency of the sampling grid
$T(k)$	–	Soft taper near $k_{\rm Nyq}$ to avoid spectral ringing
n	–	Threshold fraction defining where the high-frequency taper begins
PSD(k)	rad^2 m^2	Spatial power spectral density before tapering
PSD$_{\rm final}$(k)	rad^2 m^2	PSD after applying the Nyquist taper
$F(k,t)$	rad	Complex Fourier coefficient of the phase at frequency k and time t
Δt	s	Temporal step between successive screen updates
$\tau(k)$	s	Correlation timescale for spatial frequency k
τ_0	s	Reference correlation time at spatial frequency k_0
γ	–	Power-law exponent governing how de-correlation varies with scale
$a(k)$	–	Autoregressive damping coefficient
$\eta(k,t)$	–	Complex Gaussian noise with zero mean and unit variance
ε	–	Noise amplitude factor controlling boiling strength
$v(t)$	m s^{-1}	Advection velocity vector applied to the phase screen
v_x, v_y	m s^{-1}	Components of the advection velocity
θ	rad	Rotation angle per time step used for spiral-like flow modes
$\omega_{\rm spiral}$	rad s^{-1}	Angular drift rate governing slow rotational evolution of $v(t)$
$R(\theta)$	–	2×2 rotation matrix
$\phi(x,t)$	rad	Real phase screen in spatial domain after inverse FFT

and depends on a scale-dependent correlation time:

$$\tau(k) = \tau_0 \left(\frac{k}{k_0}\right)^{\gamma}. \tag{8}$$

The coefficient $a(k)$ represents the temporal memory of each spatial Fourier mode of the phase screen. A value $a(k) \approx 1$ (i.e., when $\tau(k) \gg \Delta t$) indicates that the corresponding spatial structure evolves slowly and retains most of its amplitude from one frame to the next, as expected for large-scale, slowly varying turbulence features. Conversely, $a(k) \ll 1$ (i.e., $\tau(k) \ll \Delta t$) means that the mode loses memory rapidly, as is typical of small-scale high-frequency fluctuations dominated by rapid de-correlation or boiling. Thus, the function $a(k)$ encodes the scale-dependent temporal stability of the turbulence and governs the balance between deterministic persistence and stochastic renewal in the phase-screen evolution. Its exponential form is physically motivated by the fact that turbulent structures in a confined dome environment exhibit approximately exponential temporal de-correlation, as expected for a stochastic process governed by linear relaxation toward equilibrium. The timescale $\tau(k)$ sets the characteristic lifetime of structures of size $1/k$: large scales (small k) persist longer, while small eddies (large k) de-correlate more rapidly.

In the temporal model, each Fourier mode evolves according to an AR(1) process with a k-dependent relaxation timescale. The coefficient $a(k)$ is chosen because if a mode with frequency k relaxes exponentially in continuous time as $dF = -F/\tau(k)\,dt$, then integrating this equation over a time-step Δt yields the exponential factor $\exp(-\Delta t/\tau(k))$. This ensures that the discrete-time model reproduces the correct physical decay rate, is stable for all choices of Δt, and reduces to the classical AR form for small time-steps. Moreover, it guarantees that modes with shorter correlation times $\tau(k)$ (typically higher-frequency structures) decay faster, whereas low-frequency large-scale structures remain coherent for longer, consistent with measurements of dome turbulence.

The exponential factor in Eq. (5) represents advection with velocity $v(t)$: corresponding to a rigid translation in real space. To model slow rotational drift of the flow, the velocity vector is rotated at each time-step:

$$v(t + \Delta t) = R(\theta)\, v(t), \tag{9}$$

where $\theta = \omega_{\rm s} \times \Delta t$, and

$$R(\theta) = \begin{pmatrix} \cos\theta & -\sin\theta \\ \sin\theta & \cos\theta \end{pmatrix}. \tag{10}$$

The parameter ω_s is the angular velocity, in radians per second, that controls the slow rotational drift applied to the advection velocity vector. It models the gradual reorientation of the airflow inside the dome, associated with slowly rotating convection cells or residual warm-air plumes. A small value of ω implies

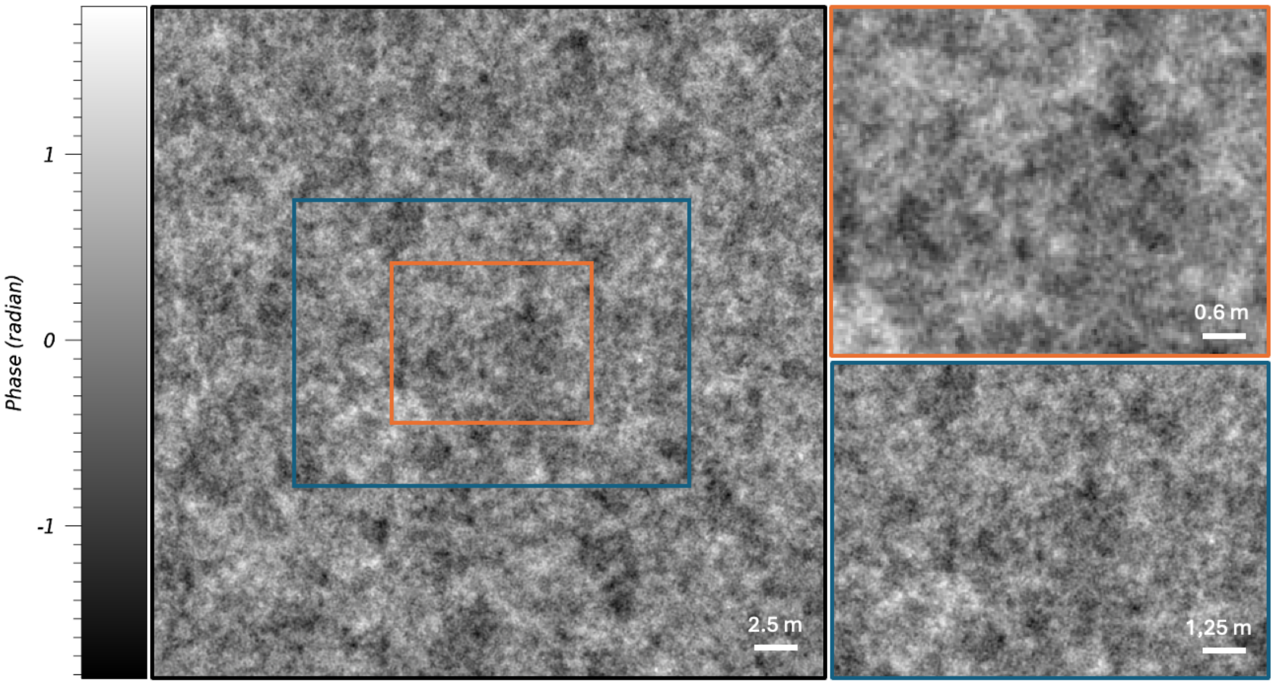

Fig. 1. Example of a phase display. The black frame shows the full phase screen. The blue frame presents a 2-times zoom of the central region. The orange frame shows a 4-times zoom of the corresponding central area.

that the velocity direction evolves only over timescales of several minutes, consistent with dome-seeing dynamics.

The stochastic noise contribution in Eq. (5) is scaled by $\sqrt{1 - a(k)^2}$, ensuring a stationary variance for each Fourier mode. This term represents non-frozen, non-translational boiling, known to be prominent inside telescope domes. To see this, consider Eq. (5) for a single mode written in the standard AR form

$$F_{t+\Delta t} = a(k)\, F_t + b\, \eta_t, \tag{11}$$

where η_t is a complex unit-variance Gaussian noise term. The variance evolves according to

$$\mathrm{Var}[F_{t+\Delta t}] = a(k)^2\, \mathrm{Var}[F_t] + b^2. \tag{12}$$

Requiring stationarity, $\mathrm{Var}[F_{t+\Delta t}] = \mathrm{Var}[F_t] = V$, implies

$$V = a(k)^2\, V + b^2 \quad \Rightarrow \quad b^2 = V\,(1 - a(k)^2). \tag{13}$$

For unit variance ($V = 1$), the unique choice ensuring a stationary process is

$$b = \sqrt{1 - a(k)^2}. \tag{14}$$

Thus, the noise amplitude must decrease when the temporal correlation coefficient, $a(k)$, is large (slow de-correlation) and must increase when $a(k)$ is small (rapid de-correlation). This scaling preserves the PSD amplitude of each spatial mode while still allowing temporal evolution, a requirement for physically realistic simulation of dome-induced turbulence where coherent drift and incoherent boiling coexist. While the advection term accounts for the slow, coherent motion of large-scale thermal structures inside the enclosure, a significant fraction of the turbulence originates from small-scale, rapidly varying convective fluctuations. These fluctuations, commonly referred to as “boiling”, are not described by a frozen-flow model. The stochastic component injects the corresponding energy into the Fourier modes, ensuring a statistically stationary variance and reproducing the observed short coherence times of dome turbulence. Finally, the updated Fourier coefficients are transformed back to real space:

$$\phi(x, t + \Delta t) = \Re\left\{\mathcal{F}^{-1}\left[F(k, t + \Delta t)\right]\right\}, \tag{15}$$

where $\mathcal{F}^{-1}$ denotes the inverse Fourier transform and $\Re$ the real part contents.

The model described in this section provides a generalized, physically motivated way to simulate dome-seeing phase screens. The spatial PSD allows non-Kolmogorov slopes, intermediate-scale bumps, and spectral tapering. The temporal model introduces scale-dependent de-correlation, weak rotation, translation, and realistic non-translational boiling. Together these elements offer a flexible framework for generating synthetic turbulence consistent dome-seeing conditions (Bustos & Tokovinin 2018; Lai et al. 2019a; Tallis et al. 2020; Munro et al. 2023). All relevant parameters used in this spatial-temporal model are synthesized in Table 1.

In practice, the proposed PSD-based spatial model and its associated temporal evolution enable the construction of multilayer dome-seeing phase screens in a straightforward manner. We can generate as many statistically independent initial phase screens as required, each sampled from the same prescribed spatial PSD but using different random Fourier phases. These screens thus represent distinct realizations of dome turbulence that share identical statistical properties. Each screen is then propagated in time using the AR-advection-noise update described above, which combines (i) partial temporal memory through the factor $a(k)$, (ii) a slow advective drift, and (iii) a stochastic boiling contribution. The resulting time series represent uncorrelated yet statistically equivalent turbulence layers located at different effective heights or regions inside the dome. Such multilayer sequences naturally reproduce the diversity of

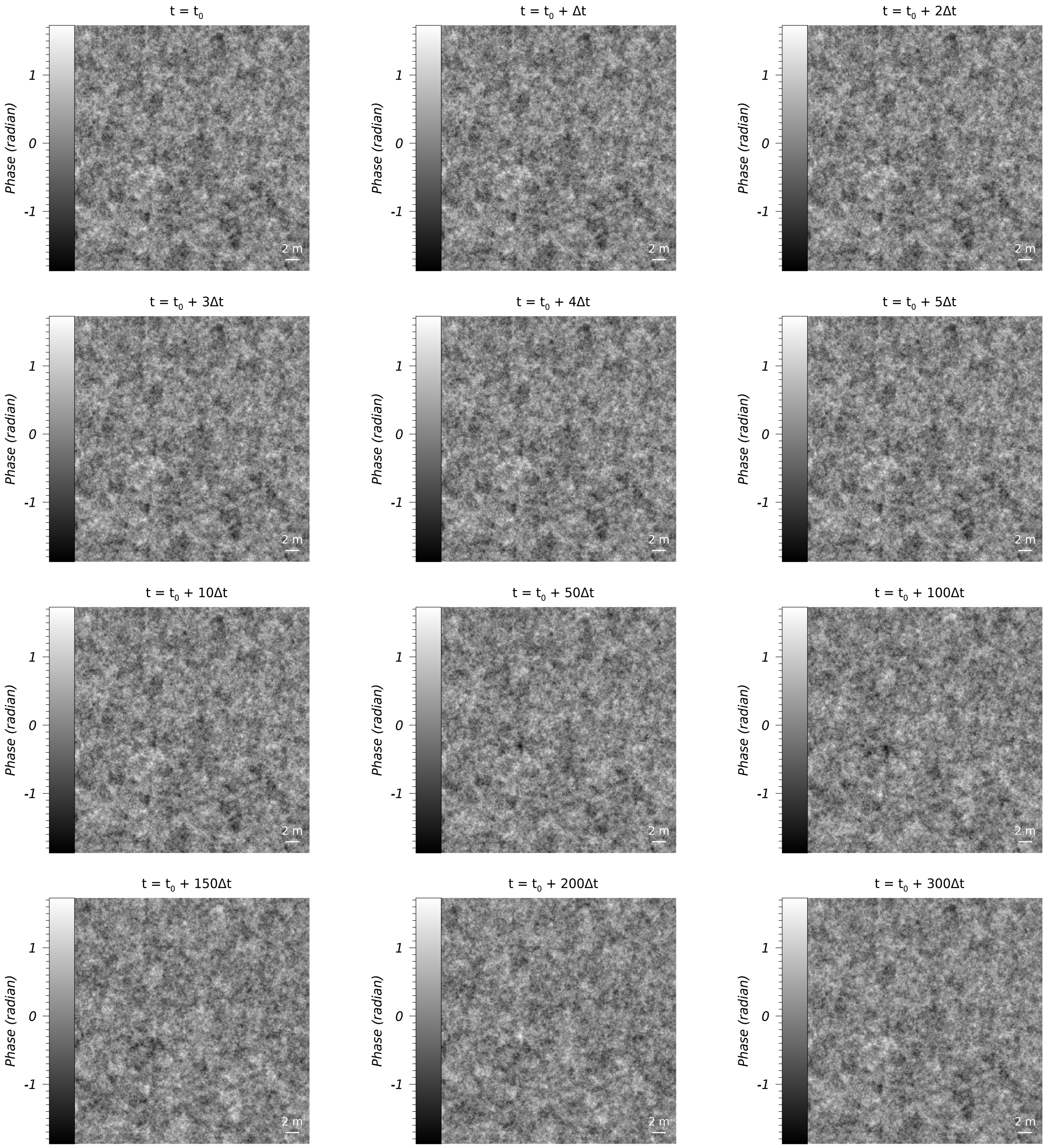

Fig. 2. Temporal evolution of a simulated dome-seeing phase screen over a total duration of 6 s. The sequence shows snapshots from t_0 to $t_0 + 300\,\Delta t$, with a temporal step of $\Delta t = 0.02$ s and a spatial sampling of $dx = 0.15$ m pixel^{-1}.

turbulent structures that coexist within a telescope enclosure and offer the flexibility to synthesize a wide range of dome-seeing regimes, from weak thermally driven fluctuations to strong mechanically enhanced turbulence.

4.3. Structure of simulated phase screens

To illustrate the spectral-temporal analytical model developed to emulate dome-seeing phase screens, we present an example simulation implemented in IDL (interactive data language) using 1024×1024 pixel phase maps with a total wavefront RMS of 30 nm. The following set of parameters was adopted: $\Delta x = 0.15$ m pixel^{-1}, $\Delta t = 0.02$ s, $k_0 = 0.12$ cycle m^{-1}, $\sigma_k = 0.02$ cycle m^{-1}, $\alpha = -2.3$, $\beta_{\mathrm{HF}} = 0.02$, $\tau_0 = 3$ s, $\gamma = 1$, $v = 0.05$ m s^{-1}, $\omega_{\mathrm{spiral}} = 0.3$ rad s^{-1}, $L_0 = 40$ m, and $l_0 = 15$ cm. A total temporal sequence of 6 s was generated. The adopted PSD slope ($\alpha = -2.3$) and advective velocity ($v = 5$ cm s^{-1}) are representative values intended to reproduce the relatively shallow spatial spectra and extremely slow thermally driven air motions typically expected inside telescope enclosures. The inner scale

(l_0 = 15 cm) was selected consistently with the weakly turbulent, low-velocity environment expected within the dome, where dissipative scales may become significantly larger than those encountered in free atmospheric turbulence. A comparatively large outer scale of L_0 = 40 m, comparable to the diameter of the European organisation for astronomical research in the southern hemisphere (ESO) ELT primary mirror, was adopted to account for the possible presence of slowly evolving thermal structures extending over a substantial fraction of the enclosure volume under weak ventilation conditions. Such a choice promotes spatial correlations across large portions of the pupil and emphasizes the low-spatial-frequency, quasi-static component of dome-seeing aberrations, which is expected to become increasingly important at ELT scales. Smaller outer scales (∼5–20 m) could alternatively be considered to represent more localized convective structures fragmented by the dome geometry, internal airflow, and mechanical infrastructure. The present choice should therefore be regarded as intentionally conservative with respect to low-order aberration content. More generally, all parameter values used throughout this work are intended as representative examples only. Their actual values are expected to be highly instrument- and site-dependent and would ultimately require dedicated in situ measurements for rigorous calibration.

The simulated dome-seeing phase screens naturally exhibit a rich multi-scale structure (Fig. 1). At large scales, the phase maps are dominated by broad, slowly varying patterns that reflect the low-frequency content of the prescribed PSD. These structures correspond to the emulation of large-scale thermal gradients and quasi-static flow features typically observed inside telescope enclosures. When zooming in (Fig. 1), the screens reveal progressively finer structures with increasingly complex spatial morphology. These high-frequency patterns arise from the non-Kolmogorov slopes imposed in the PSD and from the explicit high-frequency enhancement term used to represent mechanical and thermally driven small-scale fluctuations. This hierarchical appearance is therefore the direct visual manifestation of the broadband nature of the turbulence model. Large, slowly drifting structures reflect the dominant low-frequency energy of the dome-seeing PSD, while small-scale features exhibit stochastic fluctuations driven by the temporal de-correlation model. In Fig. 2, we show a temporal evolution of the simulated dome-seeing phase screens over a total duration of 6 s. The sequence shows snapshots from t_0 to $t_0 + 300\,\Delta t$. The spatial structure persists over time, because dome turbulence evolves slowly, but the phase sign flips because the optical path fluctuations drift around zero under slow convection and stochastic boiling; thus some patterns remain while the phase amplitude de-correlates. Together, these frames illustrate the combined effects of advection, partial temporal memory, and noise-induced boiling characteristic of dome-induced optical turbulence. In Appendix B the temporal autocorrelation of the phase-screen evolution model is discussed in detail. Appendix C provides a detailed discussion of the numerical modeling setup used to mitigate artifacts in the generation of dome-seeing phase screens, with particular emphasis on practical guidelines and key considerations for selecting appropriate spatial and temporal sampling parameters.

5. Conclusion

Dome-seeing remains an intrinsically site- and facility-dependent phenomenon, governed by the specific geometry, ventilation strategy, thermal environment, and operational configuration of each telescope enclosure. As a consequence, attempting to construct a fully generic dome-seeing model applicable to all telescopes is ultimately futile, since the dominant physical drivers vary significantly from one dome to another.

With this work, we have introduced a simplified yet physically informed model designed to emulate the spatiotemporal characteristics of turbulence inside large astronomical enclosures. The method relies on a parametrized PSD combined with a Fourier-domain temporal evolution law, enabling the controlled generation of synthetic phase screens. The approach is compact, tunable, computationally efficient, and compatible with AO simulation frameworks, and to our knowledge no such generator has ever been described in the literature. In this context, our PSD-based dome-seeing model provide a practical and self-consistent way to incorporate internal-seeing turbulence into AO end-to-end simulations: they allow dome-induced aberrations to be modeled in the same statistical framework already used for atmospheric turbulence and AO residuals, thereby enabling realistic performance predictions for AO and high-contrast instruments.

The proposed model provides a useful framework for exploring the impact of dome-seeing on AO performance and for guiding high-contrast imaging strategies aimed at mitigating the effects of internal turbulence on final contrast. It offers a more physically grounded description of dome-seeing than the stationary Von Kármán turbulence model with a reduced outer scale that is commonly used as a proxy in AO simulations. Beyond the emulation of dome-seeing itself, the framework also provides a controlled environment for testing and qualifying algorithms designed to extract dome-seeing signatures from integrated turbulence measurements, as well as for developing observational strategies and instrumental protocols dedicated to its characterization. Ultimately, the reliable identification and separation of dome-seeing contributions from atmospheric turbulence is essential for realistic AO performance simulations.

The realism of the simulations must nevertheless be assessed and strengthened through dedicated observational validation, for which targeted dome-seeing monitoring will play a particularly important role. In this context, the exploration of the model parameter space should be guided and constrained by in situ measurements to ensure physical consistency. A central challenge in confronting the proposed framework with observations is the ability to disentangle dome-induced turbulence from atmospheric contributions within integrated seeing measurements.

Consequently, at the present stage, the proposed framework should primarily be regarded as a physically motivated parameterization of dome-seeing PSD properties, introducing additional degrees of freedom linked to measurable physical processes, while the practical calibration and observational validation of these parameters remain to be demonstrated through dedicated experimental studies.

Acknowledgements. PM sincerely thanks O. Lai for insightful discussions and valuable advice on dome-seeing, as well as the anonymous referee for helpful comments and suggestions.

References

Agapito, G., Puglisi, A., & Esposito, S. 2016, SPIE Conf. Ser., 9909, 99097E
Basden, A., Wells, S., & Myers, R. 2015, in Journal of Physics Conference Series, 595, Journal of Physics Conference Series (IOP), 012002
Benedict, T. 2024, SPIE Conf. Ser., 13098, 130981S
Box, G., & Jenkins, G. 1976, Time Series Analysis: Forecasting and Control, Holden-Day Series in Time Series Analysis and Digital Processing (Holden-Day)
Bustos, E., & Tokovinin, A. 2018, SPIE Conf. Ser., 10700, 107000Q
Carbillet, M., & Riccardi, A. 2010, Appl. Opt., 49, G47
Carbillet, M., La Camera, A., Folcher, J.-P., Perruchon-Monge, U., & Sy, A. 2016, SPIE Conf. Ser., 9909, 99097J

Conan, R., Vogiatzis, K., & Fitzpatrick, H. 2024, in Optica Imaging Congress 2024 (3D, AOMS, COSI, ISA, pcAOP) (Optica Publishing Group), PTh1E.1
Ferreira, F., Gratadour, D., Sevin, A., et al. 2018, SPIE Conf. Ser., 10703, 1070347
Fétick, R. J. L., Fusco, T., Neichel, B., et al. 2019, A&A, 628, A99
Fitzpatrick, H., Conan, R., Vogiatzis, K., Das, K., & Dribusch, C. 2024, SPIE Conf. Ser., 13099, 130992I
Gratadour, D., Puech, M., Vérinaud, C., et al. 2014, SPIE Conf. Ser., 9148, 91486O
Guyon, O., Sevin, A., Gratadour, D., et al. 2018, SPIE Conf. Ser., 10703, 107031E
Jia, P., Cai, D., Wang, D., & Basden, A. 2015, MNRAS, 450, 38
Jolissaint, L., & Veran, J.-P. 2002, in European Southern Observatory Conference and Workshop Proceedings, 58, European Southern Observatory Conference and Workshop Proceedings, eds. E. Vernet, R. Ragazzoni, S. Esposito, & N. Hubin, 201
Kolmogorov, A. 1941, Akad. Nauk SSSR Dokl., 30, 301
Kornilov, V. G., Kornilov, M. V., Safonov, B. S., et al. 2025, J. Astron. Telesc. Instrum. Syst., 11, 034006
Kurmus, A., Urbach, E., & Stubbs, C. W. 2023, arXiv e-prints [arXiv:2311.03692]
Lai, O., Chun, M. R., & Withington, K. 2016, SPIE Conf. Ser., 9909, 99093H
Lai, O., Withington, J. K., Laugier, R., & Chun, M. 2019a, MNRAS, 484, 5568
Lai, O., Withington, K., Laugier, R., & Chun, M. 2019b, arXiv e-prints [arXiv:1912.02680]
Le Louarn, M., Verinaud, C., Korkiakoski, V., & Fedrigo, E. 2004, SPIE Conf. Ser., 5490, 705
Li, T., Tian, J., Wang, J., et al. 2019, J. Astron. Telesc. Instrum. Syst., 5, 024011
Marangola, M., Urbach, E., & Stubbs, C. 2025, in American Astronomical Society Meeting Abstracts, 245, American Astronomical Society Meeting Abstracts #245, 302.12
Milli, J., Kasper, M., Bourget, P., et al. 2018, SPIE Conf. Ser., 10703, 107032A
Munro, J., Hansen, J., Travouillon, T., Grosse, D., & Tokovinin, A. 2023, J. Astron. Telesc. Instrum. Syst., 9, 017004
Nicolas, S., Schwarz, H. E., & Andersen, M. I. 1998, New A Rev., 42, 441
Ogane, H., Ono, Y., Minowa, Y., et al. 2024, SPIE Conf. Ser., 13097, 1309747
Osborn, J., & Alaluf, D. 2023, MNRAS, 525, 1936
Pazder, J. S., Vogiatzis, K., & Angeli, G. Z. 2008, SPIE Conf. Ser., 7017, 70170R
Por, E. H., Haffert, S. Y., Radhakrishnan, V. M., et al. 2018, SPIE Conf. Ser., 10703, 1070342
Racine, R., Salmon, D., Cowley, D., & Sovka, J. 1991, PASP, 103, 1020
Rigaut, F. J., Veran, J.-P., & Lai, O. 1998, SPIE Conf. Ser., 3353, 1038
Roddier, F. 1981, Prog. Opt., 19, 281
Tallis, M., Bailey, V. P., Macintosh, B., et al. 2018, in American Astronomical Society Meeting Abstracts, 231, American Astronomical Society Meeting Abstracts #231, 361.18
Tallis, M., Bailey, V. P., Macintosh, B., et al. 2020, J. Astron. Telesc. Instrum. Syst., 6, 015002
Tatarskii, V. I. 1961, Wave Propagation in Turbulent Medium
Tokovinin, A. 2023, Atmosphere, 14, 1694
Tokovinin, A., Sarazin, M., & Smette, A. 2007, MNRAS, 378, 701
Vogiatzis, K., Xin, B., Claver, C., Angeli, G. Z., & Selvy, B. 2018, SPIE Conf. Ser., 10705, 1070503
Woolf, N. 1979, PASP, 91, 523
Yang, Q., Wu, X., Wang, Z., et al. 2022, MNRAS, 515, 1788
Young, A. T. 1974, ApJ, 189, 587
Zhang, Y., Xu, F., Zhuang, Y., et al. 2023, Opt. Express, 31, 40435
Zhang, Y., Lao, J., Wang, Z., et al. 2024, MNRAS, 530, 1235
Ziad, A., Conan, R., Tokovinin, A., Martin, F., & Borgnino, J. 2000, Appl. Opt., 39, 5415
Ziad, A., Borgnino, J., Dali Ali, W., et al. 2012, J. Opt., 14, 045705

Appendix A: Autoregressive temporal model

The temporal evolution of dome-induced phase screens is modeled in this work using a first-order AR process (AR(1); Box & Jenkins 1976). In this appendix we justify this choice and discuss why higher- or lower-order AR models are not appropriate for representing dome-seeing turbulence.

An AR process of order p, denoted AR(p), describes the temporal evolution of a stochastic variable as a linear combination of its p previous states plus a stochastic forcing term. In Fourier space, an AR(1) process can be written as

$$F_k^{n+1} = F_k^n\, a(k) + \sqrt{1 - a(k)^2}\, \eta_k^n, \tag{A.1}$$

where F_k^n is the complex Fourier coefficient at spatial frequency k and time step n, $a(k)$ is a scale-dependent temporal memory factor, and η_k^n is a zero-mean, unit-variance complex Gaussian noise term. This formulation corresponds to a discrete-time version of a linear relaxation process driven by stochastic forcing. The resulting temporal autocorrelation function decays exponentially,

$$R_k(\tau) \propto \exp\left(-\frac{\tau}{\tau(k)}\right), \tag{A.2}$$

with $\tau(k)$ the characteristic de-correlation timescale of structures of spatial scale $\sim 1/k$.

An AR(0) process corresponds to temporally uncorrelated (white) noise:

$$F_k^{n+1} = \eta_k^n. \tag{A.3}$$

In this case, each phase screen is an independent realization drawn from the prescribed spatial PSD, with no temporal memory between successive screens. Such a model is physically inappropriate for dome-seeing, as turbulence inside a telescope enclosure is dominated by slowly evolving thermal gradients, weak confined flows, and persistent mechanical or thermal structures. Observations consistently indicate correlation times of several seconds or longer. An AR(0) model would imply a complete renewal of the turbulent field at each time step, which is inconsistent with the confined and dissipative nature of dome-induced turbulence.

The AR(1) model represents the simplest stochastic process that includes finite temporal memory. It captures the essential physics of dome-seeing: (i) persistence of large-scale structures, (ii) gradual de-correlation due to mixing and thermal relaxation, and (iii) absence of inertial or oscillatory dynamics. The scale dependence of $a(k)$ allows larger spatial scales to persist longer than smaller ones, in agreement with physical expectations. The stochastic term accounts for local boiling effects and small-scale turbulent regeneration, while preserving a stationary variance for each Fourier mode. Importantly, the AR(1) model avoids introducing artificial oscillations or resonant behavior that are not supported by observations of dome-seeing.

Higher-order AR models, such as AR(2), introduce additional degrees of freedom corresponding to inertia or oscillatory dynamics:

$$F_k^{n+1} = c_1 F_k^n + c_2 F_k^{n-1} + \eta^n, \tag{A.4}$$

where c_1 and c_2 are the AR coefficients, controlling memory depth, damping rate, and possible oscillatory behavior. Such models can thus produce damped or sustained oscillations in time, depending on the coefficients. There is currently no observational evidence that dome-induced turbulence exhibits intrinsic oscillatory behavior or second-order temporal dynamics. Thermal plumes and confined airflow structures inside domes are primarily dissipative and relax toward equilibrium without overshoot. Introducing an AR(2) or higher-order model would therefore over-parameterize the problem and risk generating unphysical temporal correlations.

The temporal evolution of each Fourier mode in our dome-seeing phase-screen model is described by a first-order AR process (AR(1)) combined with frozen-flow advection. The AR(1) component introduces an exponential temporal de-correlation with characteristic timescale $\tau(k)$, while the frozen-flow term produces a phase rotation proportional to $k \cdot v$. As a result, the temporal autocorrelation of an individual Fourier mode (see Appendix B) takes the form

$$R_k(\tau) \propto a(k)^{\tau/\Delta t} \cos(k \cdot v\, \tau), \tag{A.5}$$

which may resemble a damped oscillation.

It is important to emphasize that this oscillatory modulation does not correspond to an intrinsic temporal oscillation of the turbulent mode. Instead, it arises purely from the kinematic effect of advecting a spatial structure across a periodic Fourier grid. The underlying stochastic process remains first-order and over-damped, with no inertia or restoring force.

Higher-order AR models, such as AR(2), naturally produce damped oscillations even in the absence of advection, as they introduce second-order temporal dynamics analogous to an under-damped harmonic oscillator. Such behavior implies wave-like or resonant temporal evolution, which is not supported by current physical understanding of dome-seeing turbulence, where fluctuations are driven by thermal gradients and mechanical mixing in a highly dissipative environment.

For these reasons, the AR(1) model provides the minimal and physically appropriate temporal description: it captures finite temporal memory and stochastic renewal of turbulent structures, while allowing apparent oscillatory features in the correlation function (see Appendix B) to arise solely from frozen-flow transport rather than from unphysical intrinsic dynamics.

In summary, the AR(1) temporal model constitutes a physically consistent description of dome-seeing evolution. It captures finite memory and exponential de-correlation while remaining numerically stable, easy to calibrate, and compatible with existing AO simulation frameworks. Lower-order models lack physical realism, while higher-order models introduce unnecessary complexity unsupported by current observational constraints.

Appendix B: Analytical temporal correlation of the Fourier-mode evolution

In this appendix we derive the temporal autocorrelation of the phase-screen evolution model used in this work and show that its AR nature associated with frozen-flow advection leads to damped oscillatory correlations.

The temporal evolution of each Fourier coefficient $F_k(t)$ is modeled as

$$F_k^{n+1} = a(k)\, e^{i\omega_k \Delta t}\, F_k^n + \sqrt{1 - a(k)^2}\, \eta_k^n, \tag{B.1}$$

where n denotes the discrete time index, Δt is the simulation time-step, $a(k) \in [0, 1]$ is the temporal memory coefficient, η_k^n is a complex white-noise process with unit variance, and

$$\omega_k = k \cdot v \tag{B.2}$$

is the frozen-flow advection frequency associated with spatial frequency k and velocity v. Equation B.1 defines a complex AR process of order one, AR(1), whose eigenvalue is

$$\lambda_k = a(k)\, e^{i\omega_k \Delta t}. \tag{B.3}$$

The temporal autocorrelation function of a stationary Fourier mode is defined as

$$R_k(\tau) = \left\langle F_k(t)\, F_k^*(t+\tau) \right\rangle, \tag{B.4}$$

with $\tau = m\Delta t$, where m is the integer time lag (number of time steps) and where U^* is the complex conjugate of the function U. Using the AR(1) frozen-flow update (neglecting noise for correlation purposes),

$$F_k^{n+m} = \left[a(k)\, e^{i\omega_k \Delta t}\right]^m\, F_k^n, \tag{B.5}$$

we obtain

$$R_k(\tau) = \left\langle F_k^n \left[a(k)\, e^{-i\omega_k \Delta t}\right]^m\, F_k^{n*} \right\rangle. \tag{B.6}$$

Because the multiplicative factor is deterministic, it can be taken outside the average:

$$R_k(\tau) = a(k)\, e^{-i\omega_k m \Delta t} \left\langle F_k^n\, F_k^{n*} \right\rangle, \tag{B.7}$$

which yields

$$R_k(\tau) = \sigma_F^2\, a(k)^m\, e^{i\omega_k \tau}, \tag{B.8}$$

where σ_F^2 is the stationary variance of the mode. Taking the real part, which governs correlations in real-valued phase screens, yields

$$\Re[R_k(\tau)] = \sigma_F^2\, a(k)^{\tau/\Delta t}\, \cos(\omega_k \tau). \tag{B.9}$$

Equation B.9 shows that the temporal correlation of each Fourier mode is the product of (i) an exponential decay envelope governed by $a(k)$, which sets the de-correlation timescale and (ii) a cosine modulation arising from frozen-flow advection. As a result, the correlation does not decay monotonically but instead exhibits damped oscillations. For low spatial frequencies (small k), where $a(k)$ is close to unity and ω_k is small, these oscillations can persist over many time-steps. When such modes dominate the PSD, their combined contribution can lead to quasi-periodic correlation decreases and increases in real-space phase-screen sequences.

Appendix C: Practical considerations

C.1. Numerical rules of thumb

The fidelity of the synthetic dome-seeing phase screens depends critically on the choice of two numerical parameters: the spatial sampling Δx and the temporal sampling Δt. These quantities control the physical scales that can be represented in the simulation and can introduce limitations in the visual or statistical realism of the resulting turbulence evolution.

In practice, the spatial sampling Δx and temporal sampling Δt must be chosen so that the simulated phase screens resolve both the relevant spatial scales of dome turbulence and its slow temporal evolution. The spatial sampling must be fine enough to resolve the smallest structures present in the prescribed PSD, while the total screen size $L = N\,\Delta x$ (N is the screen size in pixels) must remain large enough to include the lowest spatial frequencies of interest. A useful rule of thumb is that the minimum resolved wavenumber $k_{\min} \approx 1/L$ should be significantly smaller than the characteristic bump scale k_0 in the PSD, i.e.,

$$k_{\min} = \frac{1}{N\,\Delta x} \ll k_0, \tag{C.1}$$

ensuring that the large-scale dome-seeing structures are properly represented. At the same time, Δx must satisfy the Nyquist condition for the highest frequencies in the PSD and for the desired high-frequency enhancement.

The choice of temporal sampling is similarly constrained. The time step Δt must be smaller than the shortest dynamical timescale of the simulation, typically set by either the advection velocity (v) or the temporal de-correlation time ($\tau(k)$). A conservative stability and accuracy condition is

$$\Delta t << \min\left(\frac{\Delta x}{v},\ \kappa \times \tau_0\right), \tag{C.2}$$

so that (i) advective motion is not under-sampled and (ii) the AR update does not artificially inject excessive stochastic noise. In Eq. C.2, κ is a dimensionless safety factor ensuring adequate temporal sampling of the de-correlation process. If Δt is chosen too large, the noise term dominates the evolution and the phase screen appears to de-correlate too quickly, suppressing the visual advection or spiral drift that should be present. These constraints illustrate that Δx and Δt cannot be selected arbitrarily: they must jointly resolve the spatial and temporal content implied by the PSD model and the chosen drift and de-correlation parameters.

C.2. Temporal under-sampling of advected structures

This section examines a specific numerical artifact that can occur when the previously described conditions are violated, namely temporal aliasing. When phase screens are evolved using a frozen-flow or advective model, the temporal sampling must be chosen consistently with the spatial resolution of the phase screen. If the time step Δt is too large compared to the spatial sampling (Δx) and the effective advection velocity (v), numerical artifacts can appear in the form of apparent periodic repetitions of the phase pattern.

In particular, we observe cases where the phase screen pattern appears to repeat itself every $\mathcal{N}$ frames while being shifted spatially, typically in a direction opposite to the mean drift observed in intermediate frames, with a systematic spatial shift between repetitions. This behavior can be understood as a temporal under-sampling of the advected phase structure. For a dominant advective velocity component v, the phase pattern is displaced by a distance $v\,\Delta t$ at each time step. If this displacement becomes a significant fraction of the spatial sampling, the discrete representation of the screen can cause the advected structure to align repeatedly with the same pixel grid locations.

A characteristic repetition period occurs when the cumulative displacement satisfies

$$\mathcal{N}\, v\, \Delta t \simeq 2\,\Delta x, \tag{C.3}$$

which leads to

$$\mathcal{N} \simeq \frac{2\,\Delta x}{v\,\Delta t}. \tag{C.4}$$

At this cadence, the phase pattern effectively "folds back" onto the spatial grid, producing an apparent periodicity and directional aliasing in the evolution. This effect is purely numerical and does not reflect any physical periodicity of the turbulence.

To avoid this artifact, the temporal sampling must resolve the advective motion of the smallest spatial structures of interest. A practical stability criterion is

$$v\,\Delta t \ll \Delta x, \tag{C.5}$$

which is similar to what is expressed in Eq. C.2, and should be combined with Eq. C.4 ensuring that N is beyond the number of frames required. Ensuring these conditions (Eqs. C.4 and C.5) suppresses spurious pattern repetition, preserves smooth translational motion, and allows stochastic de-correlation ("boiling") to dominate the long-term evolution rather than grid-alignment effects.

C.3. Constraint on phase-screen size

Spurious revivals of temporal correlation may arise when phase screens are evolved on a finite fast Fourier transform grid with periodic boundary conditions. This effect occurs when large-scale turbulent structures, advected across the computational domain, partially overlap with their own periodic replicas. The resulting self-overlap artificially increases the similarity between phase screens separated by long time intervals, despite the intrinsic de-correlation enforced by the temporal evolution model.

To avoid this numerical artifact, the linear size of the phase screen, $L = N\,\Delta x$, must be chosen significantly larger than the largest spatial scale that contributes appreciably to the turbulence, typically set by the characteristic scale $1/k_0$ of the dominant low-frequency structures. A practical criterion is $L >> 1/k_0$, which ensures that advected structures do not re-enter the pupil through periodic wrapping over the duration of the simulation.

Equivalently, for a given advection velocity v and total simulated time $N_{\mathrm{steps}} \times \Delta t$, the screen size must satisfy

$$L \gg v\,(N_{\mathrm{steps}} \times \Delta t) \tag{C.6}$$

so that no dominant structure can traverse the full domain and overlap with its periodic copy. Failure to satisfy these conditions leads to nonphysical correlation revivals that are purely numerical in origin and should not be interpreted as physical oscillations of dome-seeing turbulence.

C.4. Quasi-periodicity induced by rotational motion

The inclusion of a weak rotational (spiral) component in the temporal evolution might introduces quasi-periodic behavior in the phase screens. This term models slow, large-scale recirculation of air within the dome, such as vortical or swirling motions driven by buoyancy and enclosure geometry. As the velocity vector is gradually rotated in time, dominant phase structures follow curved trajectories rather than purely linear advection. This can lead to partial realignment of large-scale features with their earlier configurations, producing mild revivals in temporal correlation. Physically, this behavior reflects the confined nature of dome flows, where turbulence may evolve through slow rotational drift rather than irreversible downstream transport, and is consistent with the long-lived, slowly evolving aberrations commonly associated with dome-seeing.

However, the spiral angular rate ω_{spiral} must be chosen sufficiently small to avoid artificial periodic locking of the phase structures. If $\omega_{\mathrm{spiral}}\,\Delta t$ approaches a rational fraction of 2π, dominant spatial modes can realign with their previous orientations after a finite number of time steps, producing spurious oscillations in temporal correlations. To prevent this effect, ω_{spiral} should satisfy $\omega_{\mathrm{spiral}}\,\Delta t \ll 1$ and be incommensurate with the simulation cadence, ensuring that rotational drift remains slow and non-repeating over the simulated time span. In practice, values corresponding to rotation periods significantly longer than the total simulation duration are sufficient to reproduce gentle swirling motions without introducing artificial periodicity.

To avoid artificial periodic locking induced by the spiral term, the angular rotation per time step must satisfy the previously mentioned condition, and the total accumulated rotation over the simulated duration $N_{\mathrm{steps}}\Delta t$ should remain far from integer multiples of 2π, implying a spiral period $P_{\mathrm{spiral}} = 2\pi/\omega_{\mathrm{spiral}}$ significantly longer than the simulation time. Finally, rotation-driven advection must not cause dominant turbulent structures to overlap with themselves on the finite FFT grid (see Sect. 4.5.3), requiring $vP_{\mathrm{spiral}} \ll L$. These conditions together define a narrow but well-behaved range of ω_{spiral} values that introduce slow swirling motions without generating unphysical quasi-periodic correlations.